Geomechanics and Engineering, *Vol. 41, No. 1 (2025) 129-139*
https://doi.org/10.12989/gae.2025.41.1.129

Numerical and experimental investigation into dynamic responses of permeable pipe piles in liquefiable sands

Ma Chi[1a], Mei Guo Xiong[*2], Qian Jian-Gu[**1], Shi Zhen Hao[1b] and Cheng Lin[3c]

[1]Department of Geotechnical Engineering, Tongji University, Shanghai 200092, China
[2]Ocean College, Zhejiang University, Zhoushan 316021, China
[3]Department of Civil Engineering, University of Victoria, Victoria, BC V8P5C2, Canada

(*Received October 12, 2024, Revised February 10, 2025, Accepted March 10, 2025*)

Abstract. Liquefaction of saturated sands is a leading cause of damage to roads and bridge foundations during earthquakes. To mitigate such issues, permeable pipe piles, featuring drainage holes on their shaft, have emerged as an innovative anti-liquefaction measure. However, their seismic performance in liquefiable sites has not been well understood. This study conducted both numerical and experimental tests on the dynamic response of permeable pipe piles in liquefiable sands. Before establishing the numerical model for piles, the advanced constitutive model-i.e., SANISAND adopted to the cyclic behavior of liquefiable sand was calibrated with a series of monotonic and cyclic laboratory tests. After the calibration, the numerical simulations were performed to simulate a group of shaking table tests on both traditional and permeable pipe piles in liquefiable sands. The results show that, compared with traditional pipe piles, permeable pipe piles significantly reduced liquefaction potential by dissipating excess pore water through the drainage holes, resulting in a marked decrease in pile displacement. These findings demonstrate the effectiveness of permeable pipe piles in enhancing seismic performance and provide valuable insights for their practical implementation in engineering applications.

Keywords: dynamic response; liquefiable site; numerical simulation; shaking table test; permeable pipe piles

1. Introduction

Saturated sand layers rapidly developed excess pore water pressure under earthquake loading, leading to soil liquefaction and loss of strength (Sharma et al. 2020, Shwan 2023). Implementing measures that can rapidly provide drainage channel for liquefied sand under dynamic loading conditions is an effective method to prevent liquefaction around piles (Janalizadeh and Zahmatkesh 2015, Abdullah Cheraghi and Ghorbani-Tanha 2023, Yoo and Hong 2024). Many existing technologies focus on confinement, strengthening, drainage, and densification as effective methods to reduce soil liquefaction and mitigate related damage to pile foundations (Jimenez *et al.* 2019, Khoshemehr *et al.* 2023, Zulfikar *et al*. 2023).

The development of excess pore water pressure in the surrounding soil, as illustrated in Fig. 1(a), poses significant risks to pile foundations. Since the dissipation of pore pressure can accelerate consolidation, methods to enhance this process are essential for improving the ability of traditional piles to achieve maximum resistance within a shorter time frame. In this paper, analogous to the use of vertical drains, the concept of a permeable pile is introduced as an innovative alternative to traditional piles, offering an additional drainage pathway. As depicted schematically in Fig. 1(b), drainage holes (i.e., permeable areas) can be drilled around the circumference of the pile, facilitating the dissipation of pore water pressure through these holes (Mei *et al.* 2019). During the construction of permeable pipe piles, soil surrounding the drainage holes may infiltrate the internal pipe of the pile. Additionally, the spacing between the concrete and the steel reinforcement at the drainage holes functions as a protective layer, safeguarding the reinforced concrete against corrosion. Fig. 2 show the photo of the permeable pipe pile, accompanied by precise specifications of the drain hole sizes.

The existing research on permeable pipe piles mainly focuses on the strength influence of drainage holes on the pile body and the soil compaction effect during pile driving. Laboratory tests (Ni *et al*. 2017a, Ni *et al*. 2017b, Ni *et al.* 2018, Chen *et al.* 2021) have shown that the bearing capacity of permeable piles remains pile body strength when the opening ratio of the pile surface is less than 0.5%. Theoretical analyses (Xiao *et al.* 2022, Chen *et al.* 2021) further suggest that permeable piles can enhance soil consolidation, particularly during the initial stages of consolidation. This paper aims to study the performance of the permeable pipe pile in the liquefiable sand under dynamic loading.

As widely recognized, shaking table tests and numerical simulations are effective methods for investigating the seismic response of Soil-Structure-Interaction (SSI) (Ramirez and Barrero 2018). Shaking table tests are

---

[*] Corresponding author, Professor
E-mail: meiguox@163.com
[**] Corresponding author, Professor
E-mail: qianjiangu@tongji.edu.cn
[a] Ph.D. Candidate
[b] Assistant Professor
[c] Assistant Professor

ISSN: 2005-307X (Print), 2092-6219 (Online)

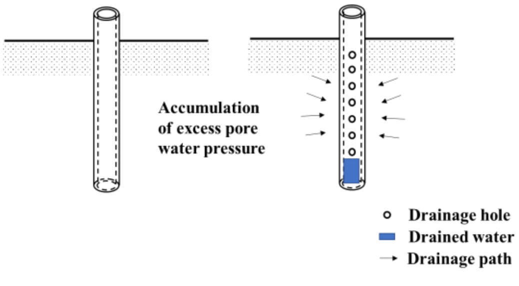

(a) (b)

Fig. 1 Schematics of the pile (a) traditional pile and (b) permeable pile

commonly employed to study various soil types, pile designs, and superstructure configurations, as they can replicate natural earthquake motions. Shaking table tests clarify the seismic response of different superstructures, the development of damage in pile foundation, and the dynamic response in soil layers (Hussein *et al*. 2022). A crucial aspect of the numerical methodology is also the accurate representation of complex soil responses under dynamic loading. The accumulation of excess pore pressure is more pronounced in looser initial states (lower densities and/or higher confinement stresses), and post-liquefaction, the sand tends to experience shear strain accumulation. Three-dimensional fully coupled effective-stress dynamic SSI analyses, incorporating both soil and pile foundation, were conducted to explore system responses and obtain reliable estimates of permeable pile foundations using the finite difference code FLAC3D (Tasiopoulou and Gerolymos 2016). It employs an explicit solution algorithm well-suited for highly nonlinear problems and supports User-Defined Models via its C++ plug-in option, facilitating accurate simulations of complex soil response patterns as anticipated use the software of in FLAC3D. Cheng (Cheng and Detournay 2021) implemented the Simple SANISAND model in FLAC 3D, developed by Dafalias and Manzari, is part of the SANISAND family of models and has been widely used to simulate the monotonic and cyclic behaviors of sands materials. The SANISAND constitutive model is grounded in bounding surface plasticity theory within the framework of critical state soil mechanics. It offers a unified description of various soil pressures and densities, incorporating fabric dilatancy effects in a multi-axial context (Dafalias and Manzari 2004). SANISAND's primary advantage lies in its ability to simulate sand's cyclic response under both drained and undrained conditions, including the stress-dependency of elastic response at very small strain ranges and the potential for soil liquefaction driven by large-strain plasticity (Reyes *et al.* 2021).

In this paper, the modification of sand cyclic stress path under SANISAND constitutive in FLAC3D. To this end, the paper first evaluates the monotonic drained and undrained comparison laboratory tests results of Nanning River sand to obtain a detailed description of the parameters. A shaking table test of the permeable pile site was conducted in liquefiable soil using micro-concrete reinforcement piles to get the dynamic performance of the permeable pipe pile. The accurately simulating the liquefaction sand to get the dynamic performance of the permeable pile by results included excess pore water pressure in soil, soil acceleration, and settlement of piles.

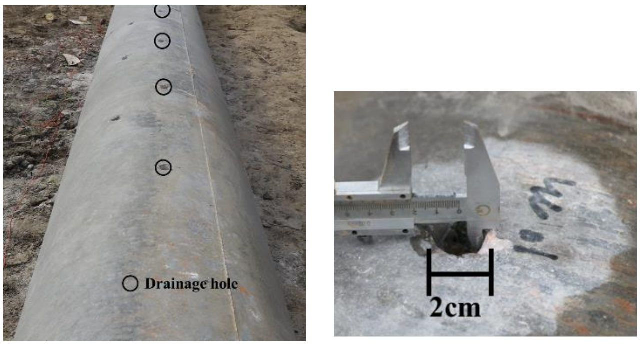

(a) (b)

Fig. 2 Photos of the permeable pipe pile(a) drainage hole position and (b) drainage hole size

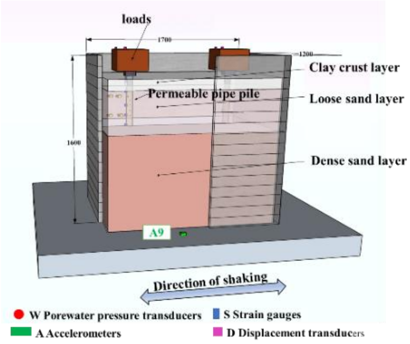

Fig. 3 The shaking table desk and the laminar shear box (unit: mm)

2. Shaking table test on the permeable pipe foundation

2.1 Geometry and boundary conditions

At Guangxi University, test was conducted on an MTS uniaxial seismic shaking table with a size of 3 × 3 m to investigate the dynamic response of the permeable pipe pile foundation. The test setup of model box, which had internal measurements of 1.5 × 1.0 × 1.6 m (length, width and height), was made up of 13 layers of steel frames to replicate the shaking of soil in a free field (Fig. 3). The height of each frame layer is 100mm, with grooves on the upper part of the frame and four wheels at the bottom. The connection between adjacent frame layers is designed such that the wheels of the upper frame are seamlessly fitted into the grooves of the lower frame, enabling smooth horizontal movement with minimal friction. A high damping rubber membrane and sponge are posted inside of the box, which cannot only prevent the leakage of soil and water but also weaken the reflections during excitations.

2.2 The model soil material

The model soil profile included three soil layers as

Table 1 Properties of tested Nanjing River sand

Parameter	Value
Density (g/cm³)	1.80
Mean particle size d_{50} (mm)	0.88
Coefficient of uniformity, Cu	4.0
Coefficient of curvature, Cc	0.69
Specific gravity, Gs	2.65
Maximum void ratio, e_{max}	0.79
Minimum void ratio, e_{min}	0.50

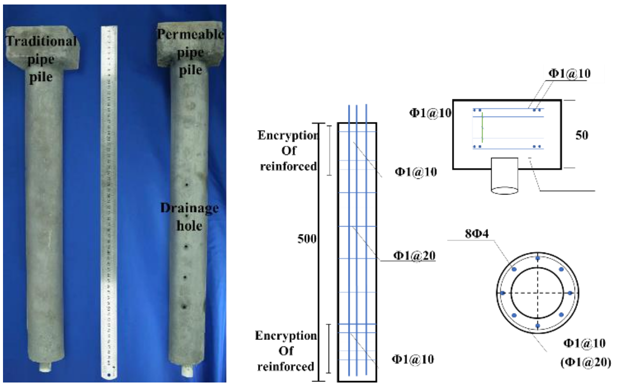

(a) (b)

Fig. 4 Model pile foundation designed for the test; (a) distributed steels in rigid bearing and piles, and (b) photo of model piles (unit: mm)

shown in Fig. 3: from the surface to the substratum are composed of 100 mm thick of clay crust, 400 mm of sand with a relative density Dr = 0.48, and overlying a bottom non-liquefiable dense sand layer with a relative density Dr = 0.78.

Table 1 summarizes the characteristics of the sand obtained from Nanning River. The accompanying clay showed natural liquid and plastic limits of 0.29 and 15.9, respectively, along with a plasticity index of 13.3. The natural density of the clay was measured at 1.68 g/cm³.

2.3 The design of the pile

Uniaxial compression tests on the concrete pile used in the shaking table test determined an elastic modulus of 18GPa for the pile, which has a diameter D = 60 mm and a pile length L = 500 mm. As shown in Fig. 4, the design reinforcement ratio of the pile meets the Chinese code and design drawings (Zhanabayeva *et al.* 2021). The connection between the pile and cap is created by the longitudinal reinforcement of the pile penetrates into the cap. The pile steels design with 4mm galvanized iron wire longitudinal reinforcement and 1mm stirrup (Zhou and Chen 2017). Five layers constitute the pile body with the permeable holes, which is located at the liquefiable layer. Each layer has four equally sized permeable holes that are 4mm in diameter.

2.4 The model soil material

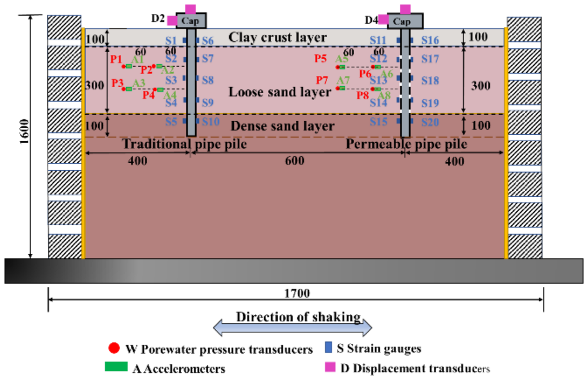

Fig. 5 Cross section of the physical model along with the layout of mounted transducers

In Fig. 5, the accelerometer and pore water pressure transducer locations, buried inside the soils, are shown, represented by symbols ‘A’ and ‘P’, respectively. They were positioned near the pile body, i.e., about 60 mm and 120 mm from the pile body side. Four accelerometers which measure horizontally (A1, A2, A3, and A4), along with four pore water pressure transducers (P1, P2, P3, and P4), were positioned to align with the two depths (the 200 mm and the 350 mm depth) in soils around the traditional pipe pile. The same to the traditional pile transducer’s position in soils, the four accelerometers (A5, A6, A7, and A8) and the four pore water pressure transducers (P5, P6, P7, and P8) in soils around the permeable pipe pile. The Displacement transducers D1 and D2 measure vertical displacement at the positioned with the center of the traditional and permeable pile cap.

2.5 Input waves and test cases

The dynamic response of SSI systems is more straightforward to analyze under sinusoidal wave excitation. Many researchers, particularly in liquefaction conditions, have utilized sinusoidal waves due to their simplicity, consistent positive and negative amplitudes, ease of analyzing time history and phase characteristics, and their alignment with the low-frequency range typical of seismic waves (Nan *et al*. 2019). In this study, a sinusoidal wave with a frequency of 5 Hz is employed as the loading condition. The waveform ramps up to peak load over 20% of its duration before and after reaching the peak, with the peak loading sustained for 14s, and the entire wave lasts for 20s. Fig. 6 illustrates this waveform, showing a peak acceleration of 0.2 g.

3. Soil constitutive models and model calibration

FLAC3D incorporates capabilities to model groundwater flow, pore water pressure dissipation, and full coupling between the deformable porous soil skeleton and viscous fluid flow within the pore space (Pham and Dias 2018, Itasca 2019). The modified SANISAND model is currently implemented in the commercially available geotechnical code FLAC3D based on the framework of the 3D finite volume numerical method. The model formulation

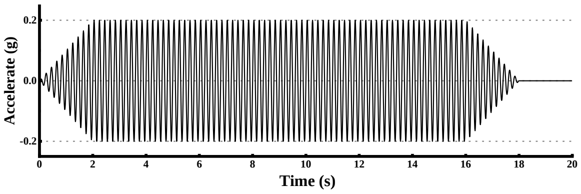

Fig. 6 Input acceleration history of calculation

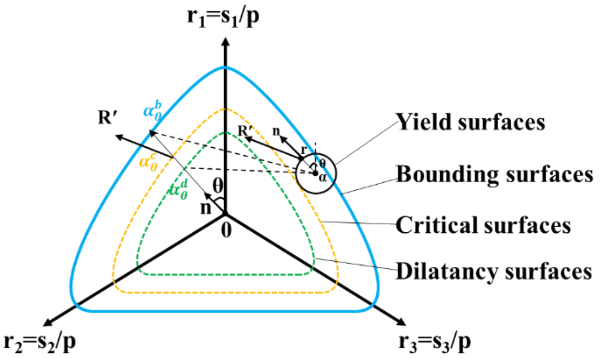

Fig. 7 Schematic illustration of model surfaces and mapping rules on the deviatoric stress ratio π in the plane

is outlined in Section 3.1. Validations of the proposed model are presented in Section 3.2. The result includes a of model results with monotonic and cyclic triaxial laboratory texts.

3.1 Model formulation

The SANISAND constitutive model can be regarded as a bounding surface model, which is an extension of their previous work by Manzari and Dafalias, which is based on the bounding surface plasticity and critical state theory frameworks and can simulate the sand response under monotonic and cyclic loading conditions (Fig. 7). A mapping rule from the origin along the unit-norm deviatoric tensor ***n***, perpendicular to the yield surface at the deviatoric stress ratio tensor r (***r***=***s***/*p*), specifies image *p*oints on the bounding surface and dilatancy surface. The purpose of the yield surface as shown in Eq. (1), which is circular, is to provide a direction of the effective stress increment, or the loading direction.

$$f = [(\boldsymbol{s} - p\boldsymbol{\alpha}):(\boldsymbol{s} - p\boldsymbol{\alpha})]^{1/2} - \sqrt{\frac{2}{3}}pm = 0 \tag{1}$$

The mean effective stress p=tr(σ)/3 is determined by the effective stress tensor σ, where tr(·) denotes the trace operator. The deviatoric stress tensor $\boldsymbol{s} = \boldsymbol{\sigma} - p\mathbf{I}$ is derived using the second-order identity tensor I. Fig. 7 illustrates the model framework, depicting surfaces and primary state variables.

The bounding surface feature renders the model capable of reverse and cyclic loading response simulation. The critical surface is defined by the triaxial compression stress ratio and serves as the reference surface for both the bounding and dilatancy surfaces. The bounding surface defines the stress state at the peak stress ratio using Eq. (2), and the dilatancy surface defines the stress state at the phase transition from contraction to dilation using Eq. (3). This updated structure of constitutive relations fully aligns with critical state soil mechanics requirements and additionally allows for the simulation of softening in dense samples.

$$M_c^b = M_c \, exp(-n^b\psi) \tag{2}$$

$$M_c^d = M_c \, exp(n^d\psi) \tag{3}$$

Where $\psi = e - e_c$, with n^b and n^d being positive material constants.

The distances from the current back-stress ratio $\boldsymbol{\alpha}$ control the plastic modulus and dilatancy, respectively. The plastic modulus is defined in Eq. (4).

$$K_p = \frac{2}{3}pb_0(\alpha_\theta^b - \boldsymbol{\alpha}):\boldsymbol{n} \tag{4}$$

The difference of current stress ratio $\boldsymbol{\alpha}$ from dilatancy stress ratio M_d, is a general function of the state variables, shown by a straight discontinuous line in Fig. 7. This is also known as the phase transformation line. A contract (D>0), dilatant (D<0), or zero volumetric rate (D=0) response is obtained from the Eqs. (5) and (6).

$$D = A_d\left(\boldsymbol{\alpha}_\theta^d - \boldsymbol{\alpha}\right):\boldsymbol{n} \tag{5}$$

$$A_d = A_0(1 + \langle \boldsymbol{z}:\boldsymbol{n} \rangle)\left(\boldsymbol{\alpha}_\theta^d - \boldsymbol{\alpha}\right) \tag{6}$$

where D is the dilatancy; and A_d is the positive material constants; z is the fabric tensor; ⟨ ⟩ is Macaulay's bracket. The term ⟨ ⟩ accounts for the fabric change effect on the dilatancy behaviour.

According to the macroscopic observations about the desired change of D along with the foregoing micromechanical observations lead to the following proposition. The fabric-dilatancy internal variable z is defined as Eq. (7).

$$d\boldsymbol{z} = -c_z\langle -d\varepsilon_v^p \rangle(z_{max}\boldsymbol{n} + \boldsymbol{z}) \tag{7}$$

It is important to emphasize that the evolution of z occurs only when $d\varepsilon_v^p$<0, i.e., during the dilatant phase of shearing. This will leave intact the value of A_d for loading which remains entirely in the contractive phase, thus facilitating the specification of A_0 from corresponding data before z is activated.

While the above equation was shown to be effective for monotonic loading, it has not overcome two shortcomings of the SANISAND model during cyclic loading: one is the repeating stress-path without further increases in shear strain amplitude after some cycles; the other is the overly high damping ratio at relatively large shear strain. Recalling the great advantage of bounding surface plasticity to define at will the coefficient of K_p (as long as K_p = 0 on the bounding surface), and to improve cyclic performance, two supplementary factors f1 and f2 are added into the formula for the modified model:

$$K_p = \frac{2}{3}ph_0f_1f_2D_rG\frac{(\boldsymbol{\alpha}_\theta^b - \boldsymbol{\alpha}):\boldsymbol{n}}{(\boldsymbol{\alpha} - \boldsymbol{\alpha}_{in}):\boldsymbol{n}} \tag{8}$$

where f_1 and f_2 are functions introduced to improve performance.

$$f_1 = \frac{100(1-f_r)}{100 + q\varepsilon_{eq}^{p}} + f_r \tag{9}$$

f₁ is a degradation factor of plastic stiffness and is introduced to eliminate the phenomenon of repeating stress-path without further increases in shear strain amplitude.

f₂ is introduced mainly to improve the cyclic performance of post-liquefaction and is defined by

$$0.1 \le f_2 = \left(\frac{p}{p_z}\right)^{(1-Dr)} \le 1 \tag{10}$$

However, due to recognized limitations in predicting pore pressure rates quantitatively, the numerical values obtained in this study should primarily be considered qualitatively and comparatively. Nonetheless, the observed general trends are believed to hold.

3.2 Validation tests with SANISAND parameter calibration

Monotonic drained and undrained comparison laboratory tests (test CD and test CU) were performed on isotopically consolidated sand samples. The samples were prepared using either the moisture placement or wet tamping method within a mold measuring 50 mm in diameter and 120mm in height. Before each test, the dimensions of the samples, enclosed within a 0.3-mm latex membrane, were recorded along with their dry unit weight. Carbon dioxide was applied to the sample under a low pressure of 3.5 kPa for approximately 10 minutes, followed by deaired water flushed into the sample through bottom drain lines under a cell pressure of 20 kPa. All tested samples exhibited average B-values (Zamani *et al*. 2023) exceeding 0.96 after backpressure saturation.

Fig. 8 compares simulation results with laboratory data from drained and undrained triaxial compression tests conducted on isotopically consolidated sand samples at confining pressures of *p*=50kPa and *p*=100kPa. Fig. 3 presents results from triaxial compression tests on isotropically consolidated sand, showing changes in drainage conditions from drained to undrained. The initial relative densities (*Dr*) for the simulation cases, *Dr* =0.22,0.36,0.48, and 0.55 in undrained comparison, represent loose to dense sands, respectively (Do *et al.* 2023). For the drained condition, the case with a relative density of 0.48 was selected.

Fig. 9 compares the experimental stress path and stress–strain path with the numerical results obtained with modified SANISAND model for *Dr* = 0.48, respectively. The modified SANISAND response is performance well agreement with the experimental curves and fully captures the cyclic mobility features of sand during loading, reverse loading, and the post-liquefaction stage. This capability overcomes one of the main shortcomings of the SANISAND model, which instead exhibits deadlock path loops without further accumulation of shear strain at zero effective stress. The simulation results demonstrate SANISAND's capability to accurately match experimental data for monotonic and cyclic loading in both drained and undrained triaxial compression tests on isotopically consolidated sand samples. Table 2 lists parameters derived from the results of monotonic drained and undrained triaxial tests.

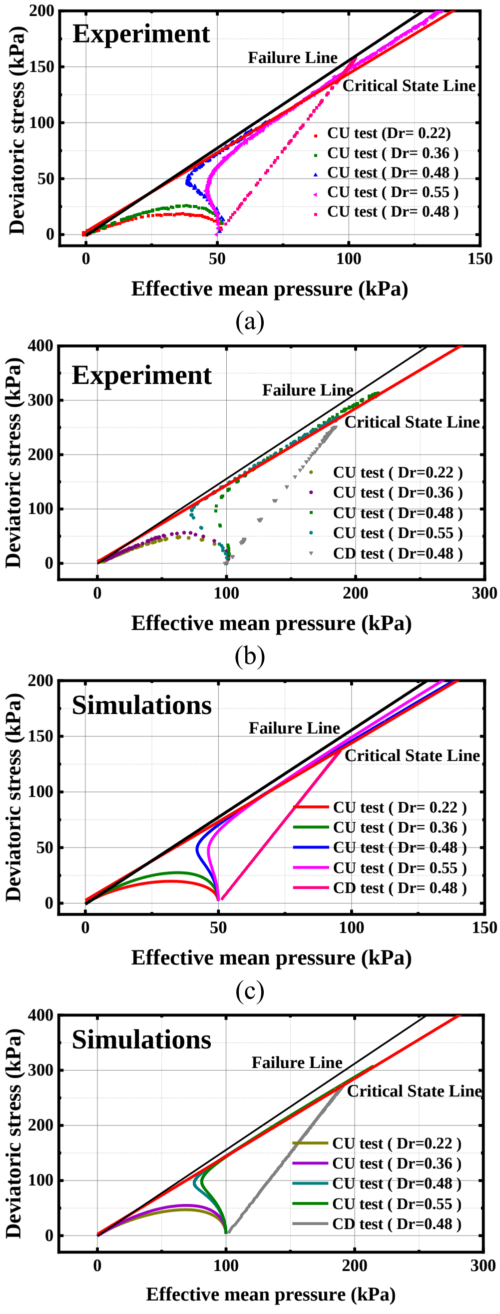

Fig. 8 Deviatoric stress versus effective mean pressure in drained and undrain triaxial compression tests on Nanning River sand: (a) and (b) experimental data of initial effective mean pressure p = 50 and 100 kPa; (c) and (d) numerical simulation results with SANISAND of initial effective mean pressure p = 50 and 100 kPa

From the cyclic loading results find that a general shortcoming and a lack of calibration flexibility for separate pre- and post-liquefaction response simulations. The shortcoming is the use of a quantity related to cumulative plastic volumetric or shear strain in their formulation for dilatancy determination or stiffness degradation that stays in

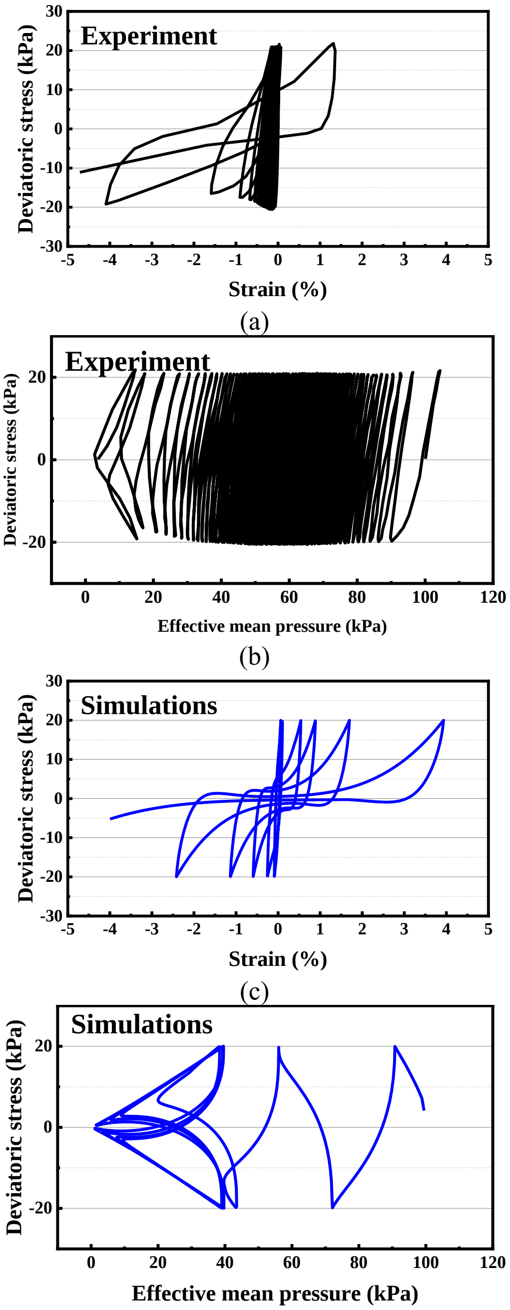

(a)

(b)

(c)

(d)

Fig. 9 Deviatoric stress versus strain (left) and versus mean pressure (right) in undrained hollow cylinder cyclic torsional tests of sand for relative density Dr = 0.48; (a) and (b) experimental data; (c) and (d) numerical simulation results with SANISAND

the model after the completion of a cyclic loading process, based on the non-decreasing nature of a cumulative quantity. It is noteworthy that the SANISAND constitutive model demonstrates remarkable capability in characterizing the stress-strain relationship of sand under cyclic loading conditions. This model successfully simulates two critical aspects: the mean effective stress (*p*) approaching zero and the distinctive butterfly-shaped stress path, both of which are consistently observed in experimental data.

Table 2 Summary of model parameters for the SANISAND constitutive model in FLAC3D

Parameters		Value
Elasticity	Elastic material constant, G0	1250
	Poisson's ratio, ν	0.05
Critical-state	Critical-state stress ratio M	0.3
	State line constant, λc	0.2
	Void ratio at p = 0, e_0	0.934
	State line constant, ξ	0.3
Plastic modulus	Plastic shear rate, h_0	7.05
	Boundary constant, n^b	1.25
Dilatancy	Plastic volumetric rate, A_0	0.4
	Dilatancy constant, n^d	0.7
Fabric-dilatancy	Maximum fabric magnitude, z_{max}	2
	Date of fabric, c_z	800

4. Test results and model simulations

Three dimensional fully coupled effective stress dynamic SSI. This section presents a description of the shaking table test sand the simulation of the permeable pipe pile foundation in FLAC3D.

4.1 Description of numerical modeling

Considering the large difference between pile and soil stiffness, which will affect the calculation time of the model, the soil grid is only encrypted near the pile, and the calculation mesh is shown in Fig. 11. The soil mesh is constituted by 6440 brick zones and 40 wedge zones. The dimensions of volume of soil considered in this study are 1.6×1.0×1.5 m (length, width, and height). The profile is composed of 3 layers, where the layer in between corresponds to the 0.3-m-thick liquefiable soil and the other layers do not. The water table of the mesh is located at the surface of the numerical mesh. The free-field boundary is imposed on the sides of the mesh in order to simulate the soil nature deposits accurately.

Mechanical aspects of concrete in FLAC3D are represented by an elastic constitutive model to simulate concrete pile. Table 3 shows the material parameters of the pile used in FLAC3D. The reinforced concrete pile was modeled using solid elements.

Potential foundation-soil separation or slippage was simulated using interface elements placed between the pile and the soil. In FLAC3D, these interface elements follow an elastic-perfectly plastic force-displacement law defined by elastic stiffness and strength parameters. Normal to the interface, representing potential separation, the strength is defined by a tensile limit. Parallel to the interface, simulating potential sliding, a Mohr-Coulomb failure criterion is applied based on cohesion and an interface friction angle. Following sensitivity analyses, high values were assigned to both normal and shear stiffness parameters

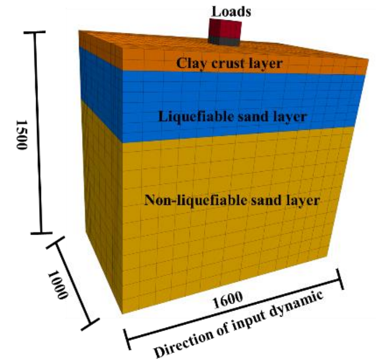

Fig. 10 Geometry of the numerical model (unit: mm)

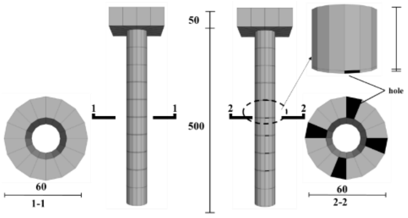

(a) (b)

Fig. 11 3D mesh for the simulation pile; (a) traditional pipe pile, and (b) permeable pipe pile (unit: mm)

Table 3 Material properties of the soil-pile interface

Parameter	Value
Elastic modulus (GPa)	20
Compressive strength (MPa)	32.5
Tensile strength (MPa)	1.9

Table 4 Material properties of the soil-pile interface

Parameter	Value
Normal stiffness (GPa)	16
Shear stiffness (GPa)	16
Friction	20

to prevent excessive strain in the interface elements. Given the cohesionless nature of the soil beneath the slab, the interface elements were assigned zero tensile strength and cohesion, approximately matching the friction angle of the underlying soil under rough contact conditions. The calculations and analyses are conducted based on the schemes outlined in Table 4. In the numerical simulation, contact surfaces are set at the pile-soil interfaces, including around the pile, at the pile bottom, and between the pile cap and the soil. For traditional pipe pile foundations, the contact surfaces are modeled with an impermeable condition, while for permeable pipe piles, the contact surfaces at the openings are modeled with a permeable condition.

Compared to the traditional pipe pile, the permeable pile features five layers of equally spaced holes in its body. The permeable hole area of the permeable pipe pile is the same as the circular hole area with a diameter of 4mm using in shaking table test. These holes are drilled around the circumference of the pile to facilitate drainage at the soil-pile interface. Modeling the pile structure with solid elements enables a more accurate simulation of its structural characteristics and the drainage effects of these holes.

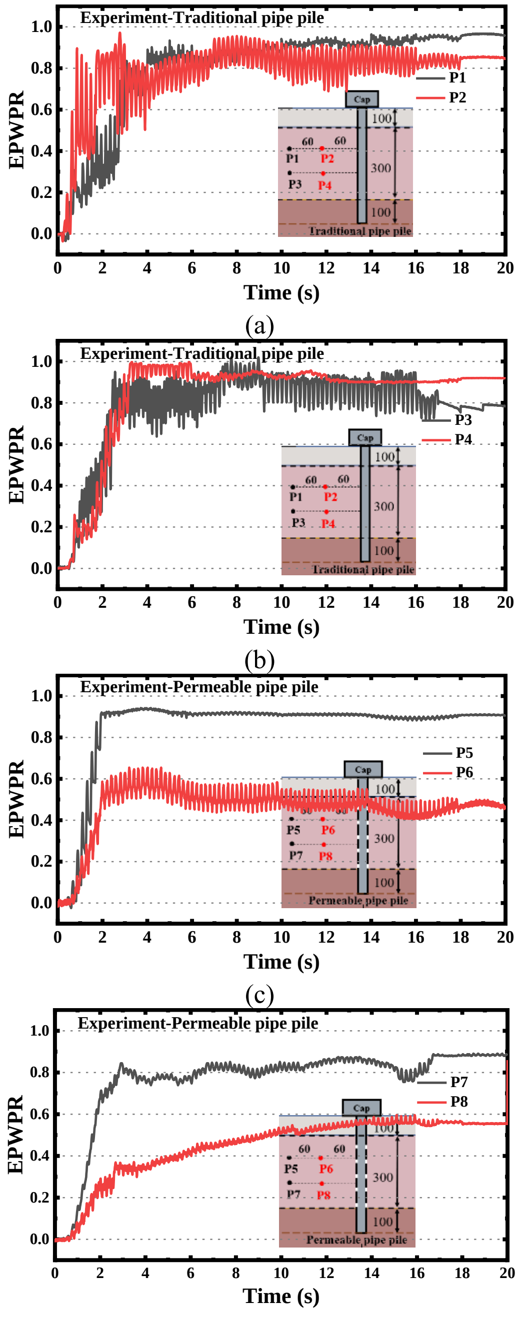

(a)

(b)

(c)

(d)

Fig. 12 EPWPR time histories obtained experimentally at four locations (unit: mm)

4.2 Soil response

The excess pore water pressure ratio (EPWPR), defined as the ratio of the difference between current pore water pressure and initial pore water pressure to the mean initial effective stress (σ_0'), is utilized to quantify the variation of pore water pressure in soil. Figs. 12 and 13 compare experimental and numerical results regarding excess pore

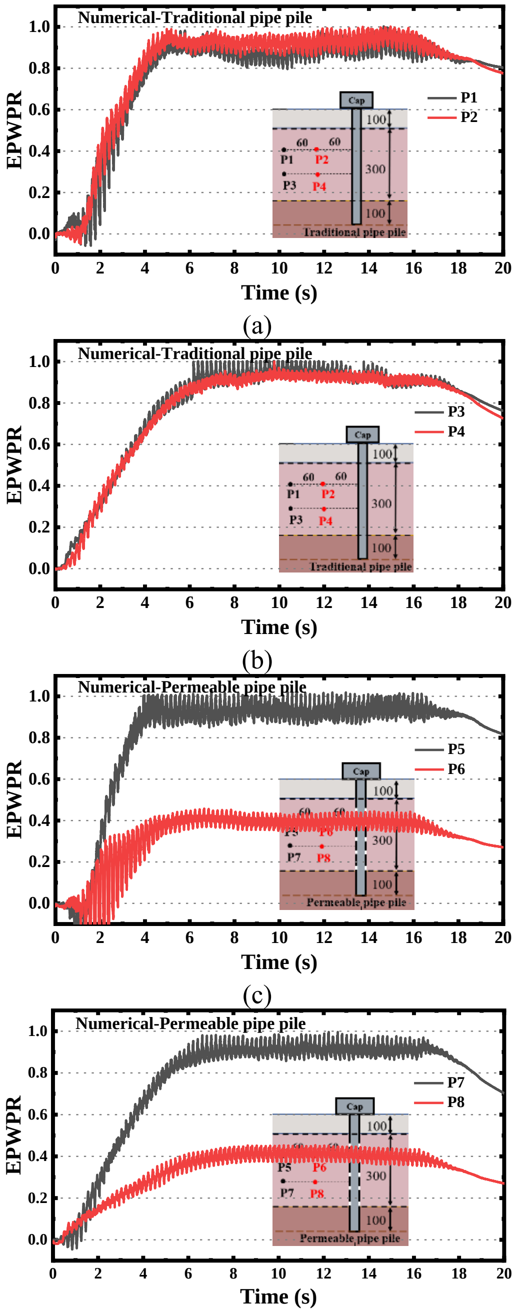

(a)

(b)

(c)

(d)

Fig. 13 EPWPR time histories obtained numerically at four locations (unit: mm)

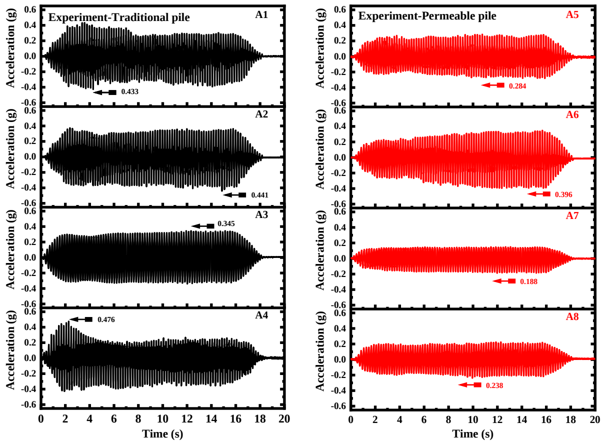

(a) (b)

Fig. 14 Acceleration time histories obtained experimentally at four locations

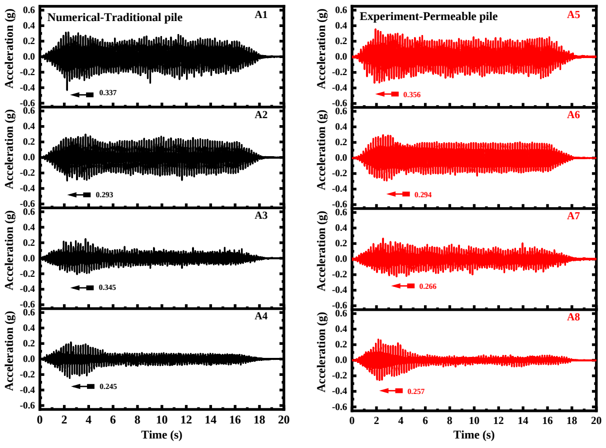

(a) (b)

Fig. 15 Acceleration time histories obtained numerical at four locations

water pressure ratio time histories at selected locations for both traditional and permeable pipe pile foundations at measurement points P1-P8. As shown in Figs. 12(c) and 12(d), and Figs. 13(c) and 13(d), the liquefiable sand layer quickly develops significant excess pore pressures under dynamic loading. In all cases, numerical and experimental data exhibit good agreement.

Fig. 12 displays the EPWPR after dynamic loading for the traditional pipe pile foundation. It also presents time histories of EPWPR at two different elevations within the liquefiable sand for both the traditional and permeable pipe pile foundations. Around the traditional pipe pile, the soil excess pore water pressures accumulate rapidly early during shaking (at t≈2.0s) and quickly stabilize at EPWPR≈1.0, indicating complete soil liquefaction. In contrast, the soil around the permeable pipe pile experiences partial liquefaction with the EPWPR≈0.6–0.9. However, at a horizontal distance approximately twice the pile diameter from the pile body (X = 2.0D), the EPWPR in the sand still develops quickly, the loss of drainage effectiveness provided by the permeable pipe pile.

Fig. 13 presents simulated results of EPWPR time histories at two different elevations (as shown in Fig. 5(c)), compared with shaking table test data. Figs. 8(a) and 8(b) demonstrate that excess pore pressures reached similarly high levels, consistent with experimental results. Around the traditional pipe pile, soil excess pore water pressures begin early during shaking and quickly stabilize at EPWPR≈1.0, indicating complete soil liquefaction.

Figs. 13(c) and 13(d) show similar early development and stabilization of EPWPRs during shaking. The soil the EPWPR around a horizontal distance of approximately 1 time the pile diameter (X = 1.0D) from the pile, the EPWPR generation is at a low level and stabilized in 0.4. Additionally, the EPWPR in the sand soil remains below

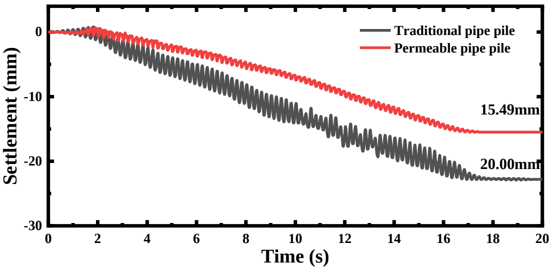

Fig. 16 Experimentally measured settlement time histories at pile cap

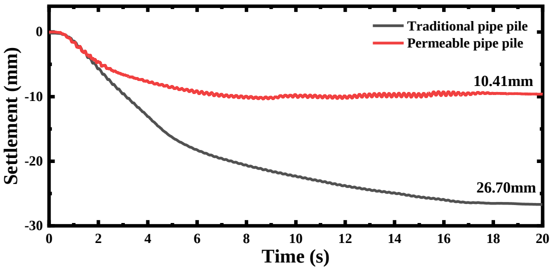

Fig. 17 Numerically computed settlement time histories at pile cap

liquefaction levels depicted in Figs. 8(c) and 8(d). However, when the horizontal distance from the soil to the pile body reaches 2 times the pile diameter (X = 2.0D), the EPWPR stabilizes at a very high value (EPWPR = 1.0), the soil is in a liquefied state, and the drainage effect of the permeable pipe pile disappears.

Figs. 14 and 15 depict the experimentally measured and numerically computed acceleration time histories at various depths. Both simulations generally agree with the measured response, albeit with some discrepancies. In the traditional pile foundation, the accelerations decrease in amplitude with increasing embedment depth, consistent with previous shaking table test findings on liquefaction (Mikhailova *et al.* 2009, Zhang *et al.* 2022). This reduction in acceleration amplitudes is particularly notable in the shallow layers of the sand (at depths of 200 mm and 400 mm). The exact cause of this decrease remains uncertain, though it may stem from slight densification and settlement of the model during shaking.

Similarly, in the permeable pile foundation, a reduction in acceleration amplitude is observed. Compared to the traditional pile foundation, there is a noticeable decrease in acceleration amplitude in the upper layer surrounding the permeable pipe pile. This reduction is primarily attributed to decreased accumulation of excess pore pressure, which in turn increases the stiffness of the sand.

Fig. 15 displays the numerically computed acceleration time histories at various depths for the SANISAND models. While both simulations generally agree with the measured response, there are some discrepancies noted. Specifically, the numerical simulations tend to underpredict accelerations at the frequency of the input motion. Ramirez *et al.* (2018) observed similar discrepancies in their simulations using SANISAND models.

4.3 Pile response

As shown in the Fig. 16, settlement accumulation progresses as the cap rocks during seismic activity. The settlement was suddenly increased at the time around 2s. Post-seismically (after time around 18s), reconsolidation of liquefied layers contributes to further settlement stabilization. The settlements of the pile cap decrease to approximately 15.49 mm compared to 20 for the traditional pipe pile by the end of the seismic motion. The increased permeability of the permeable pile appears to play a crucial role in significantly reducing pore pressure, thereby contributing to decreased settlement.

The time of reaching liquefaction state is also verified by the settlement curves. As seen by Fig. 17. The settlement was suddenly increased at the time around 2s, which was due to onset of liquefaction in traditional pipe pile foundation. The maximum value of settlement reached 26.70 mm, and at the same time, the value of settlement decreased to 10.41 mm in permeable pipe pile foundation. However, due to shortcomings of SANISAND including the overpredicting the buildup rate of pore pressures, this comparison should be considered in a qualitative manner.

5. Conclusions

This study presents numerical simulations of the shaking table test to analyze the performance of permeable pile foundations reinforced the liquefied sand. The simulations utilized the modify SANISAND constitutive model to capture the cyclic response of liquefied sand. A comparative analysis with traditional pile foundations was conducted based on the response of both the pile and the surrounding soil. The findings demonstrate that permeable pipe piles exhibit enhanced capability in preventing or delaying liquefaction compared to traditional pipe pile foundations.

The initial calibration phase focused on obtaining stress-strain responses from a comprehensive set of monotonic and cyclic fully drained and undrained triaxial tests. The constitutive model's behavior and the materials of Nanning River sand of SANISAND were further elucidated through simulations of element loading tests under varying confining stresses (50 kPa and 100 kPa), initial relative densities of sand (Dr = 0.22,0.36,0.48, and 0.55) and cyclic loading scenarios of sand relative density Dr = 0.48 of using in the shaking table. The model was validated by laboratory experiments. The SANISAND constitutive model parameters obtains from the monotonic and cyclic simulated which suitable for Nanning sand.

After calibration, dynamic loading simulations were conducted on a shaking table test. These simulations successfully replicated key system responses, including soil EPWPR, soil acceleration, and pile settlement. The results show that the soil EPWPR generation is at a low level and stabilized around the permeable pipe pile (X =1.0D). This was attributed to the permeable pipe pile holes that can serve as drainage channels allowing it to be drained during an earthquake. In the horizontal direction, a low amplification factor of acceleration from the soil near the permeable pipe pile was obtained, due to the decrease in excess pore pressure accumulation, which leads to an increase in the stiffness of the sand. Comparing the traditional pile and the permeable pile cap displacement showed that the permeable pile cap has a less displacement. It was concluded that soil shows more resistance against liquefaction through the response of the permeable pipe pile foundation compared to the traditional pipe pile.

Acknowledgments

The support provided by the National Natural Science Foundation of China (Project No.52178321) is gratefully acknowledged; Fundamental Research Funds for the Central Universities (Grant No. 20232ZD08).

References

Chen, Z., Xiao, T., Feng, J., Chen, D. and Chen, Y. (2021), "Mathematical characterization of pile–soil interface boundary for consolidation analysis of soil around permeable pipe pile", *Can. Geotech. J.*, **58**(9), 1277-1288. https://doi.org/10.1139/cgj-2020-0337.

Cheng, Z. and Detournay, C. (2021), "Formulation, validation and application of a practice-oriented two-surface plasticity sand model", *Comput. Geotech.*, **132**, 103984. https://doi.org/10.1016/j.compgeo.2020.103984.

Cheraghi, A. and Ghorbani-Tanha, A.K. (2023), "Numerical analysis of an innovative expanding pile under static and dynamic loading", *Geomech. Eng.*, **32**(4), 453-462. https://doi.org/10.12989/gae.2023.32.4.453.

Dafalias, Y.F. and Manzari, M.T. (2004), "Simple plasticity sand model accounting for fabric change effects", *J. Eng. Mech.*, **130**(6), 622-634. https://doi.org/10.1061/(ASCE)0733-9399(2004)130:6(622).

Do, T.M., Laue, J., Mattsson, H. and Jia, Q. (2023), "Excess pore water pressure generation in fine granular materials under undrained cyclic triaxial loading", *Int. J. Geo-Eng.*, **8**(1). https://doi.org/10.1186/s40703-023-00185-y.

Hussein, A.F. and El Naggar, M.H. (2022), "Effect of model scale on helical piles response established from shake table tests", *Soil Dyn. Earthq. Eng.*, **152**(6), https://doi.org/10.1016/j.soildyn.2021.107013.

Itasca Consulting Group Inc. (2019), FLAC3D (Fast Lagrangian Analysis of Continua in 3 Dimensions), version 7.1. Minneapolis, Minnesota, United States.

Janalizadeh, A. and Zahmatkesh, A. (2015), "Lateral response of pile foundations in liquefiable soils", *J. Rock Mech. Geotech. Eng.*, **7**(5), 532-539. https://doi.org/10.1016/j.jrmge.2015.05.001.

Jimenez, G.A.L., Dias, D. and Jenck, O. (2019), "Effect of layered liquefiable deposits on the seismic response of soil-foundations-strcture systems", *Soil Dyn. Earthq. Eng.*, **24**, 1-15. https://doi.org/10.1016/j.soildyn.2019.05.026.

Khoshemehr, G.A. and Bahadori, H. (2023), "Investigating the dynamic response of deep soil mixing and gravel drain columns in the liquefiable layer with different thickness", *Geomech. Eng.*, **34**(6), 665-681. https://doi.org/10.12989/gae.2023.34.6.665.

Li, N., Men, Y., Yuan, L., Wang, B. and Liu, X.(2019), "Seismic response of micropiles-reinforced landslide based on shaking table test", *Geomatics, Nat. Hazards Risk*, **10**(1), 2030-2050. https://doi.org/10.1080/19475705.2019.1664643.

Mei, G., Xu, M., Wu, W., Li, Y., Zhao, Y. and Zhang, Z. (2019), "Water-permeable pipe pile system capable of accelerating soil consolidation and method of using the same", US10309072B2.

Nguyen, A.D., Nguyen, V.T. and Kim, Y.S. (2024), "Finite element analysis on dynamic behavior of sheet pile quay wall dredged and improved seaside subsoil using cement deep mixing", *Int. J. Geo-Eng.*, **15**(1). https://doi.org/10.1186/s40703-023-00186-x

Ni, P.P., Mangalathu, S., Mei, G.X. and Zhao, Y.L. (2017 b), "Compressive and flexural behaviour of reinforced concrete permeable piles", *Eng. Struct.*, **147**, 316-327. https://doi.org/10.1016/j.engstruct.2017.06.007.

Ni, P.P., Mangalathu, S., Mei, G.X. and Zhao, Y.L. (2017a), "Permeable piles: An alternative to improve the performance of driven piles", *Comput. Geotech.*, **84**, 78-87. https://doi.org/10.1016/j.compgeo.2016.11.021

Ni, P.P., Mangalathu, S., Mei, G.X., and Zhao, Y.L. (2018), "Laboratory investigation of pore pressure dissipation in clay around permeable piles", *Can. Geotech. J.*, **55**(9), 1257-1267. https://doi.org/10.1139/cgj-2017-0180.

Pham, H.V. and Dias, D. (2018), "3D numerical modeling of a piled embankment under cyclic loading", *Int. J. Geo-Eng.*, **19**(4). https://doi.org/10.1061/(ASCE)GM.1943-5622.0001354.

Ramirez, J., Barrero, A.R., Chen, L., Dashti, S., Ghofrani, A., Taiebat, M. and Arduino, P. (2018), "Site response in a layered liquefiable deposit: Evaluation of different numerical tools and methodologies with centrifuge experimental results", *J. Geotech. Geoenviron. Eng.*, **144**(10), 04018073.1-04018073.22. https://doi.org/10.1061/(ASCE)GT.1943-5606.0001947.

Reyes, A., Yang, M., Barrero, A.R. and Taiebat, M. (2021), "Numerical modeling of soil liquefaction and lateral spreading using the SANISAND-Sf model in the LEAP experiments", *Soil Dynam. Earthq. Eng.*, **4**, 143. https://doi.org/10.1016/j.soildyn.2021.106613.

Sharma, N., Dasgupta, K. and Dey, A. (2020), "Optimum lateral extent of soil domain for dynamic SSI analysis of RC framed buildings on pile foundations", *Front. Struct. Civil Eng.*, **14**(1), 62-81. https://doi.org/10.1007/s11709-019-0570-2.

Shwan, B.J. (2023), "Microstructural interpretation of effective stress equations for unsaturated sands", *Int. J. Geo-Eng.*, **23**(1), 1-9. https://doi.org/10.1186/s40703-022-00181-8.

Tasiopoulou, P. and Gerolymos, N. (2016), "Constitutive modelling of sand: A progressive calibration procedure accounting for intrinsic and stress-induced anisotropy", *Géotechnique*, **66**(9), 1-17. https://doi.org/10.1680/jgeot.15.P.284.

Xiao, T., Ni, P., Chen, Z., Feng, J., Chen, D. and Mei, G. (2022), "A semi-analytical solution for consolidation of ground with local permeable pipe pile", *Comput. Geotech.*, **143**, 104590. https://doi.org/10.1016/j.compgeo.2021.104590.

Yoo, M. and Hong, S. (2024), "Evaluation of dynamic earth pressure acting on pile foundation in liquefiable sand deposit by shaking table tests", *Geomech. Eng.*, **38**(5), 487-495. https://doi.org/10.12989/gae.2024.38.5.487.

Zamani, S., Lajevardi, S.H. and Yarivand, A.Z.E. (2023), "Experimental study of the behavior of square footing on reinforced sand with treated geotextile", *Int. J. Geo-Eng.*, **14**(1), 1-15. https://doi.org/10.1186/s40703-023-00195-w.

Zhanabayeva, A., Sagidullina, N., Kim, J., Satyanaga, A. and Moon, S.W. (2021), "Comparative analysis of Kazakhstani and European design specifications: Raft foundation, pile foundation, and piled raft foundation", *Appl. Sci.*, **11**(7), 3099. https://doi.org/10.3390/app11073099.

Zhang, X., Dong, X. and Russell A.R. (2022), "Liquefaction responses of fiber reinforced sand in shaking table tests with a laminated shear stack", *Soil Dynam. Earthq. Eng.*, **162**(11), 1-16. https://doi.org/10.1016/j.soildyn.2022.107466.

Zhou, Y. and Chen, P. (2017), “Shaking table tests and numerical studies on the effect of viscous dampers on an isolated RC building by friction pendulum bearings”, *Soil Dynam. Earthq. Eng.*, **100**, 330-344. https://doi.org/10.1016/j.soildyn.2017.06.002.

Zulfikar, R.A., Yasuhara, H. and Kinoshita, N.P.H. (2023), “Utilization of carrageenan as an alternative eco-biopolymer for improving the strength of liquefiable soil”, *Geomech. Eng.*, **33**(1-2), 221-230. https://doi.org/10.12989/gae.2023.33.2.221.